Lasers in Manufacturing and Materials Processing
https://doi.org/10.1007/s40516-023-00241-6

RESEARCH

CO_2 Laser Sintering of TiO_2 Nanoparticles Thin Films for Improved Transmittance

Yahya Bougdid[1,2] · Francois Chenard[3] · Chandraika (John) Sugrim[4] · Ranganathan Kumar[2] · Aravinda Kar[1]

Accepted: 15 December 2023

Abstract

Photothermal CO_2 laser sintering of anatase titanium dioxide (TiO_2) nanoparticles (NPs) is reported in this paper for depositing transparent TiO_2 thin films on quartz substrates. Drops of TiO_2 NPs suspension are spread on the substrates using a spin-coating technique to prepare wet TiO_2 thin films of different thicknesses in a controlled manner. These wet films are subsequently heated with a CO_2 laser ($\lambda = 10.6\ \mu m$) in two stages, corresponding to the drying process for evaporating the liquid of the nanoparticles suspension and the sintering process for bonding the nanoparticles to form a transparent TiO_2 film. The microstructures of the spin-coated (wet), dried, and sintered TiO_2 films have been studied using optical and scanning electron microscopy (SEM). The optical transmittance of the films is characterized by UV/Vis/NIR spectrophotometry and fourier-transform infrared (FTIR) spectroscopy. The transmittance of the sintered TiO_2 films increased nearly linearly over the ultraviolet (UV) to visible (Vis) range of wavelengths and reached an average transmittance above $\sim 92\%$ in a certain infrared (IR) range, *e.g.* at 2500 *nm* wavelength, and their transparency is slightly affected by the film thickness. The X-ray diffraction (XRD) analysis revealed that the sintered TiO_2 films are polycrystalline with an anatase crystal structure, without the appearance of any traces of the rutile phase of TiO_2.

Keywords Anatase TiO_2 · Spin-coating · CO_2 laser sintering · Transparent TiO_2 films · Transmittance · Structural properties

✉ Aravinda Kar
akar@creol.ucf.edu

[1] Center for Research and Education in Optics and Lasers (CREOL), The College of Optics and Photonics, University of Central Florida, Orlando, FL 32816, USA

[2] Department of Mechanical and Aerospace Engineering, University of Central Florida, Orlando, FL 32816, USA

[3] IRflex Corporation, 300 Ringgold Industrial Parkway, Danville, VA 24540, USA

[4] Naval Air Warfare Center, Aircraft Division, Patuxent River, MD 20670, USA

Published online: 06 January 2024

Introduction

For many technologies, nanoparticles (NPs) are the raw material for manufacturing functional materials and devices [1, 2]. Recently, titanium dioxide (TiO_2) has been the subject of sustained research interest due to its biocompatibility, chemical, and biological stability, and wide bandgap (3.2 eV) semiconductor properties [3, 4]. TiO_2 exists in three different crystalline phases: anatase (tetragonal), brookite (orthorhombic), and rutile (tetragonal) [4]. Anatase is the dominant phase at low temperatures due to its thermodynamic stability, and it is considered the most applicable phase of TiO_2 in solar cells due to the most efficient mobility of electrons [3, 5]. Rutile is also a stable phase as a bulk material with denser crystalline structure and greater refractive index [6]. Anatase can be obtained from amorphous TiO_2 in the temperature range 350 $°C$-550 $°C$ [3], and it transitions to the stable TiO_2 rutile phase at ~600 $°C$ [7]. Transparent TiO_2 films have been extensively used for various applications due to their exceptional and unique characteristics, such as non-toxicity, high refractive index, and wide spectral range of optical transparency [6–8]. The advantages of transparent TiO_2 films as self-cleaning glasses and coating on lenses have been reported recently [6]. Transparent TiO_2 thin films prepared by the laser sintering process play a crucial role in the coating of optics, enhancing the durability and performance of various optical components and devices [9, 10]. Transparent TiO_2 films can be used to create optical coatings, such as anti-reflective coatings (ARCs) on lenses for high power laser applications [6, 10], self-cleaning [11], and ARCs for solar cell [12, 13]. The TiO_2 coatings can reduce unwanted reflections by minimizing the amount of light that is bounced back from the surface of the devices. ARCs are commonly used on camera lenses, eyeglasses, and other optical devices to improve image quality and visibility [9, 10]. Application of TiO_2 ARCs in optoelectronic devices is also reported [14]. Transparent TiO_2 films can be applied as protective coatings on optical devices to prevent abrasion, chemical damage, and scratching [15]. Transparent TiO_2 thin films are engineered to have specific mechanical, chemical, and optical properties tailored to the requirements of each application [3, 5, 9].

Compared to the expensive and complex laser nanofabrication techniques [16–19], the spin-coating deposition followed by laser sintering technique used in this study, and nanoelectrospray laser deposition (NELD) [20–22] methods offer a cost-effective, and scalable process for depositing, patterning, and sintering microstructures using different suspensions of nanoparticles. Sta et al. [23] utilized spin coating followed by annealing in a furnace; however, Schade et al. [8] used spin coating followed by laser sintering to prepare transparent TiO_2 films. Spin-coating of TiO_2 nanoparticles followed by laser-assisted sintering has many advantages for our research, including low process costs, the production of thin as well as thick and multiple-layer homogeneous and heterogenous films of uniform thickness, and the ability to prepare highly transparent TiO_2 films with compact and porous morphologies [11, 23]. The limitation and comparison of existing methods and how the NELD process overcomes them have been discussed

in [20]. Spin-coating followed by laser sintering is suitable for depositing highly uniform thin films [8, 24]. Also, laser processing allows localized heating at high temperatures without heating the entire substrate, whereas the entire substrate is heated in the case of sintering the film in a furnace [21]. Therefore, the laser-assisted thin film deposition can be applied to thermally sensitive substrates. In the patterning process, the laser can be scanned on the spin-coated films to sinter only along the track of the laser beam, and the unscanned portion can be washed away. These sintered tracks can be designed for constructing optical gratings for different wavelength ranges, such as mid-wave infrared light.

The sintered TiO_2 films exhibit an enhancement in the optical, and structural properties depending on the laser processing conditions [3, 21]. Schade et al. [8] sintered TiO_2 NPs on soda-lime glass substrates using a 355 *nm* laser and studied the effect of the laser power on the sintered grain size. Radovic et al. [25] examined the effect of laser energy on the mechanical and electrical properties of screen-printed TiO_2 films. Annealing of the TiO_2 films causes surface energy variation and migration of atoms, resulting in the growth of crystalline microstructures [4]. At an annealing temperature of 300 $°C$, TiO_2 begins to crystallize into the anatase phase, and at 900 $°C$, it starts to transform into the rutile phase [26]. Bakri et al. [26] annealed TiO_2 films at 500 $°C$ and their XRD analysis detected a tetragonal anatase structure with a preferred growth orientation along the (101) plane. UV–Vis spectrophotometry of sintered TiO_2 films showed a high transmittance between 70% and 90% in the visible region according to [9, 11, 23]. In our study, the choice of a CO_2 laser instead of common UV or Vis lasers to sinter TiO_2 nanoparticles is due to the ability of 10.6 μm laser wavelength to provide efficient and deep sintering through the film depth [21]. Ming et al. [5] reported that the UV laser energy can only be absorbed by the top ultrathin (~200 *nm*) layer of TiO_2 films, leading to a heavily melted top layer of the sintered nanoparticles. The thermal annealing in a furnace can also be applied to sinter TiO_2 nanoparticles to produce transparent films [26]. Cheng et al. [27] reported a mathematical model describing the laser densification of ceramic, and they showed that the heat-affected depth in the film is 50 μm from the surface. This theoretical study showed that the laser can be used as an effective heat source for sintering and densification of different nanoparticles. Uniform sintering, however, cannot be achieved by short laser wavelengths since the TiO_2 films possess very high absorptance in the UV range [3].

In our study, a 10.6 μm laser with an optimized combination of processing parameters is used to prepare transparent anatase TiO_2 films on the quartz substrates. A heat transfer model is used in this study to select the proper laser processing parameters, *i.e.,* laser power and scanning speed, for controlling the phase transformation and sintering of TiO_2 nanoparticles. The effect of different processing conditions, *e.g.,* the revolution per minute (RPM) for spin-coating deposition, and the laser evaporation and sintering conditions, on the morphological, optical, and structural properties of the wet and sintered TiO_2 films are presented. Scanning electron microscopy (SEM) shows that the spin-coated wet films can be sintered with an enhancement in the microstructural properties. A theoretical model is also developed to correlate the final thickness (h_{SI}) of the sintered film with the deposition RPM. Spectrophotometry measurements show that the transmittance of the sintered

TiO_2 films is slightly affected by the film thickness. XRD analysis and spectrophotometry of the sintered TiO_2 films exhibit pure polycrystalline anatase structures and high transmittance, respectively.

Experimental Procedure

Spin-Coating Deposition of TiO_2 Wet Films

A nanosuspension of 20 *wt.%* anatase TiO_2 nanoparticles of 18 *nm* size in ethylene glycol (EG) was used in this study. TiO_2 Nanoparticles (anatase, 99.9%) of 18 *nm* size and powdery polymer dispersant were purchased from US Research Nanomaterials, Inc. The nanosuspension was prepared by adding 20 *wt.%* TiO_2 NPs to EG. 5 *wt.%* of the dispersant was added to prepare homogenous suspension. The clusters size in the suspension was not measured, however, the ultrasonic process operated at 80 *kHz* for 20 *min* gives a homogenous suspension for preparing uniform films. Prior to wet deposition of TiO_2 films, the fused quartz substrates were ultrasonically cleaned as detailed in [21]. For wet deposition, a drop of 0.1 mL suspension is dispensed onto the substrate which is positioned on the stub of the spin–coater (Laurel WS-650 Hz-23NPP). The TiO_2 drop was spread on the quartz substrate by initially applying 500 RPM for 5 *s* during the initial spinning phase followed by different higher RPMs for 25 *s* to control the thickness of the wet films. This 500 RPM will be referred to us the acceleration RPM to conform with the terminology of the spin-coating device since the input 500 RPM is displayed as "Acel: 500". After the initial spinning stage at 500 RPM, the thickness of the TiO_2 coating is determined and controlled in the second stage; *i.e.,* deposition stage [28]. In the deposition stage, the spin coater accelerates the rotation speed (deposition RPM) to a higher value, *i.e.,* from 2000 RPM to 11000 RPM.

Optical System for CO_2 Laser Processing

A CW (continuous wave) CO_2 laser of wavelength $\lambda = 10.6\ \mu m$ was used to sinter the wet films obtained in the above-mentioned spin-coating process (Fig. 1(b)). The

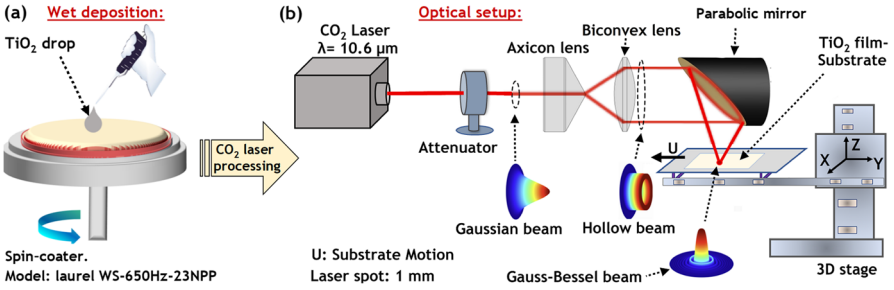

Fig. 1 **(a)** Spin-coating deposition of wet TiO_2 films. **(b)** Schematic illustration of the optical system for CO_2 laser processing

laser beam passes through several optical elements (Fig. 1(b)), changing the original Gaussian beam of the laser source to an annular cylindrical beam of a nearly uniform radial irradiance distribution. A hollow parabolic mirror is used to transform the annular cylindrical beam into an annular conical beam and to create a focused or defocused laser spot on the sample. At the focal point of the parabolic mirror, *i.e.,* at the apex of the cone, the diameter of the laser spot is 300 μm in this study. The original Gaussian beam transforms into a Gauss-Bessel beam with an irradiance distribution different from the typical Gaussian Irradiance distribution. The laser beam is defocused to change its diameter from 300 μm to 1 *mm* for avoiding any cracks in the sintered TiO_2 films. The laser heating process is completed in two steps: (i) pre-heating of the wet film at 1.1 *W* laser power to evaporate EG and (ii) sintering of TiO_2 nanoparticles in the relatively dry film at 2 *W*. The substrate is moved beneath the laser beam using a 3D stage at the speed of 2.5 *mm/s* for pre-heating and 2 *mm/s* for sintering steps.

Characterization

The surface morphology of TiO_2 films was characterized using a Zeiss Ultra-55 FEG SEM (Scanning Electron Microscopy) and an optical microscope (Nikon, Japan). Before SEM analysis, the TiO_2 samples were coated with a thin gold layer of thickness 1 *nm* to prevent the charging effects during the interaction between the e-beam of SEM and the samples. The crystalline structure of the TiO_2 films were determined using an XRD Basic Diffraction PANalytical Empyrean. The XRD data were recorded at the angle 2θ in the range of 10° to 80° by scanning the samples in steps of 0.05525° increments for 1 *sec* per step. An Agilent Cary 5000 UV–VIS-NIR Spectrophotometer and a Perkin Elmer-Spectrum-2 Fourier transform infrared (FTIR) spectrometer were used to measure the optical transmittance. The thickness of TiO_2 films was determined with a Bruker DEKTAK XT profilometer.

Theoretical Models

Theoretical Model 1: Processing Parameters Selection

Laser sintering of TiO_2 nanoparticles necessitates a careful selection of laser processing parameters, aiming to achieve efficient sintering, and preventing substrate cracking [29]. To prevent the loss of TiO_2 nanoparticles during the drying step, we selected the appropriate power and scanning speed corresponding to the temperature for evaporating EG liquid of the wet film. First, the thermophysical properties of the 20 *wt.*% TiO_2 suspension were determined by applying the mixture rule. The absorptance of EG was previous determined in [21] based on the EG data reported in [30]. Table 1 presents the thermophysical properties of TiO_2 suspension and its compositions.

For both pre-heating (drying of EG) and sintering steps, the temperature required to evaporate EG and subsequently sinter nanoparticles is estimated to be the

Table 1 Thermal and optical properties of TiO_2 nanoparticles (NPs), ethylene glycol (EG), and the mixture 20 *wt.*% TiO_2 NPs in EG [21, 29]

	Thermal Conductivity (k) $[W/(m \cdot K)]$	Thermal Diffusivity (α) $[10^{-6} m^2/s]$	Absorptance at 10.6 μm (A) [%]
TiO_2 NPs	8.4	5.06	55
Ethylene glycol	0.258	0.11	97
TiO_2 NPs + EG	1.886	1.10	88.6

temperatures at the laser-material interaction zone on the surface of the sample [31, 32]. This temperature is obtained by developing a heat transfer theoretical model as we previously detailed in [21]. The calculated temperature strongly depends on the thermophysical proprieties of the TiO_2 suspension (Table 1) and the laser processing parameters. Using our model [21], 1.1 *W* power at 2.5 *mm/s* was selected to evaporate EG. The sintering temperature is calculated as a function of power for different scanning speeds, as shown in Fig. 2(a). Determining the derivative of temperature with respect to the time, we also calculated the rate at which the temperature rose per unit of time, *i.e.*, heating rate, during the laser processing to minimize the laser thermal effect on the samples [31, 32].

As shown in Fig. 2(a), 2 *mm/s* combined with a minimum power (~2 *W*) were chosen to minimize the heating effect of laser on the sample, thus minimizing the loss of TiO_2 nanoparticles. Shown in Fig. 2(b) is the cooling rate, which determines how fast the substrate is cooling down as a function of the laser [31, 32]. The model used for calculating the temperature, heating, and cooling rate was previously detailed in [21]. As indicated in Fig. 2(b), a power of 2 W at 2 *mm/s* was chosen to get a slow cooling of the sample and prevent its breakage, and simultaneously, sinter TiO_2 films. 2-2.5 *W* power at 2 *mm/s* speed gives rise to a temperature of ~350 – 425°*C* [21]. It was previously reported [26, 33] that the annealing of TiO_2 films at 350°*C* showed the appearance of the crystallin anatase phase.

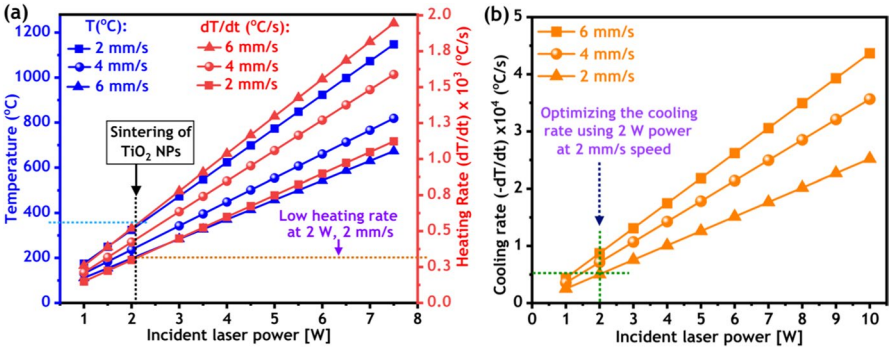

Fig. 2 **(a)** Calculated temperature (blue scatters) and heating rate (red scatters) as a function of laser power for different scanning speeds. **(b)** Calculated cooling rate as a function of power for different scanning speeds

Theoretical Model 2: Dependency of Sintered Film Thickness (h_{SI}) on the Deposition RPM

J. D. Flores et al. [34] presented the following equation for the film thickness (h_{sc}) obtained after the spin-coating deposition, as given below:

$$h_{SC} \approx \left[0.85.\, x_0 .\, \frac{\rho_{\,solv}}{\rho_{\,solute}} \,.\, \left[\frac{\upsilon\, D^{\frac{1}{2}}_{solv,air}\, P^{*}_{solv}\, M_{solv}}{\rho_{\,solv} \upsilon R_g\, T} \right]^{\frac{1}{3}} \right] \omega^{\,-\frac{1}{2}} \;\approx\; K_{SC} \omega^{-\frac{1}{2}} \qquad (1)$$

where x_0 is the volume ratio between solute and solvent in the initial solution, υ is the kinematic viscosity, ω is the rotational velocity ($radian/s$) for deposition, ρ_{solv} is the density of solvent, and ρ_{solute} is the density of solute.$D^{1/2}_{solv,air}$,P^{*}_{solv}, M_{solv}, R_g and T denote the diffusion coefficient of the solvent in air, the vapor pressure of the pure solvent, molecular weight of solvent, the ideal gas constant, and the temperature of the suspension, respectively [34]. The factor K_{SC} depends on the characteristics of the suspension drop which is dispensed to the substrate before starting the spin-coating process.

In our study, the spin-coated wet film is sintered with a laser beam and, therefore, the thickness of the sintered film (h_{SI}) is expected to be less than h_{SC} *i.e.*,$h_{SI} < h_{SC}$, due to the densification of the film during sintering at 2 W [29]. The laser sintering process depends on the initial thickness h_{SC} of the wet TiO_2 film, the temperature, and the heating and cooling rates induced by the laser beam [21]. These thermal effects depend on the irradiance of the laser absorbed by the material, the relative motion between the laser spot and the substrate, *i.e.,* the laser scanning speed, and the thermophysical properties such as the density, specific heat capacity and thermal conductivity of the deposited film and the substrate [29]. To relate h_{SI} to the deposition RPM used for producing h_{SC}, the following expression is considered as a first order approximation.

$$h_{SI} = K_{SI} \omega^{-m} \qquad (2)$$

where the factor K_{SI} depends on K_{SC}, the laser processing parameters and the thermophysical properties as mentioned above. Since $h_{SI} < h_{SC}$, the value of m is expected to be greater than 1/2. Figure 3 presents the log–log graph showing the measured final thickness (h_{SI}) as a function of deposition RPM.

Compared to Flores et al.'s work [34] in which the slope of the straight line in the thickness h_{SC} (wet film thickness) versus the spin coating speed graph is -1/2, our result shows the dependency of h_{SI} (thickness after laser sintering) on the deposition RPM. It is clearly seen that the magnitudes of the two slopes in Fig. 3 are greater than 1/2 because the dependance of h_{SI} on ω may be ω^{-m} with $m > 0.5$. Also Fig. 3 indicates that the exponent can be constant over a certain range of ω and may vary over larger range of ω. The results show, as a first order approximation, that it is possible to predict the thickness of the sintered TiO_2 films by optimizing the process parameters for spin-coating wet deposition.

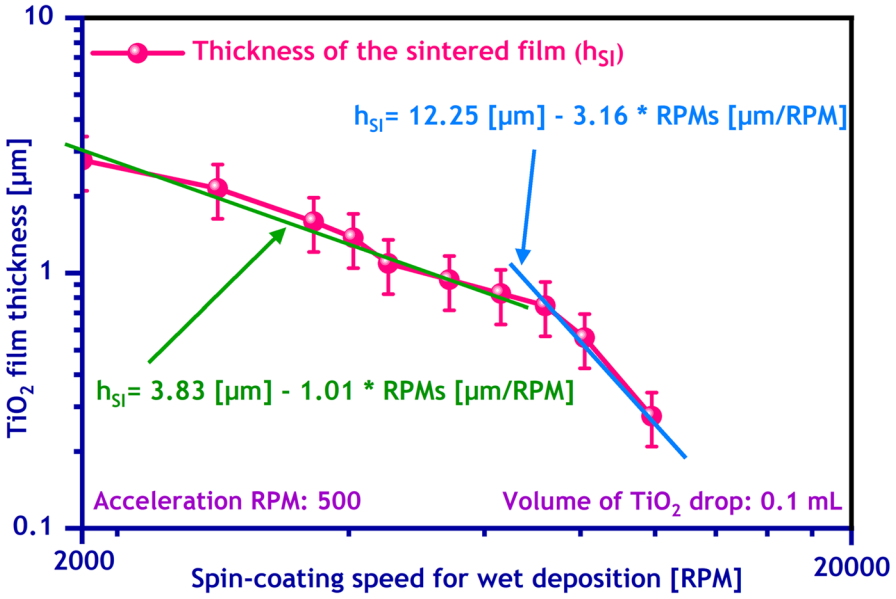

Fig. 3 Log–log graph showing the measured thickness of the sintered TiO_2 films as a function of deposition RPM (*i.e.,* from 2000 RPM to 11000 RPM). A power of 2 *W* at 2 *mm*/*s* was used for sintering these films

Results and Discussion

Optical Analysis of Chuck Mark, Striations in TiO_2 Films and Transmittance of Different Film Portions

During the coating of TiO_2 suspension, the viscosity of the suspension dominates the thinning forces in the spread-out drop and the evaporation of liquid dominates the coating thinning behavior [28, 35]. Several defects can be appeared on the wet films after spin coating deposition such as the chuck mark, and striations. Relatively thicker wet film is formed on the substrate at the central region that covers the vacuum chuck of the spin coater, and this particular thick portion is referred to as the chuck mark [28]. The chuck marks are created by the thermal energy transfer between the TiO_2 wet film deposited on top of the substrate and the back side of the substrate on top of the vacuum chuck. This mark appears due to the temperature differences between the liquid suspension, quartz substrate and the chuck. The evaporation of the liquid that carries the nanoparticles may also contribute to the formation of the chuck marks [28]. Shown in Fig. 4(a) is a picture of a TiO_2 wet film deposited on a quartz substrate at 2000 RPM. Figure 4(b) presents the film shown in Fig. 4(a) after laser sintering. It is clearly observed in Fig. 4(b) that the TiO_2 film (2.76 μm) (thickness) become transparent after evaporation of EG and sintering of nanoparticles. The film was scratched using a sharp diamond pen, and the 2.76 μm thickness was measured from the scratch (substarte surface) to the top surface of the sintered film.

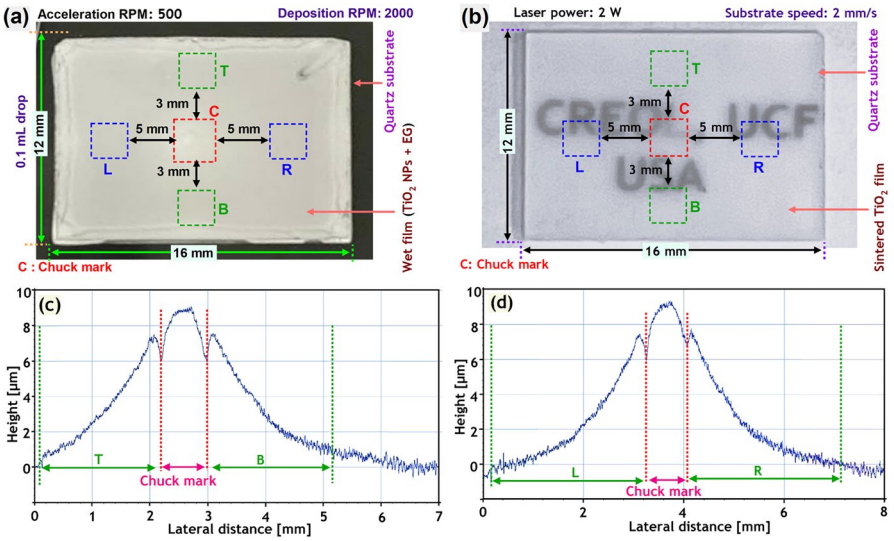

Fig. 4 **(a)** A picture of a wet film deposited on a quartz substrate. **(b)** A picture of a sintered TiO_2 film on a quartz substrate. Profilometry measurements of the chuck marks height in the sintered TiO_2 film: **(c)** from top to bottom, and **(d)** from left to right of the chuck mark

We studied the morphological and optical properties of this sintered film (Fig. 4(b)) in five (T: top, B: bottom, C: center, L: left, and R: right) regions. The center of this film shows a thick white dot of 1.5 *mm* diameter, representing the chuck mark. The profilometry analyses of the film height from the top surface of the sintered film are presented for T to B regions in Fig. 4(c) and for L to R regions in Fig. 4(d). The measured height of the chuck mark is ~8.64 μm above the top surface of the sintered TiO_2 film. The diameter of the chuck mark was determined to be ~1.5 *mm*, and in some cases, the diameter is the same as that of the spin-coater chuck.

The acceleration and deposition RPMs affect the thickness and quality of the wet films. We examined the effect of the acceleration on the quality of the wet TiO_2 films, as shown in Fig. 5. For acceleration of 50 RPM and deposition RPM of 2000, azimuthal and radial striations were observed around the chuck mark (Fig. 5). We also observed that a low acceleration of 50 RPM influenced the size of the chuck marks. For example, chuck marks of diameters 0.63 *mm*, 1.5 *mm* were obtained for 50 RPM, and 500 RPM acceleration, respectively. Minimal striations were observed when the acceleration was 500 RPM, and this RPM was used as the initial rotational (spinning) speed for 5 *s* in our other experiments.

The morphology of the sintered TiO_2 film at various locations that are identified as T, C and L in Fig. 4(b) is investigated. Each of the location pairs T and B, and L and R is assumed to have similar morphology. The surface of the wet TiO_2 film in Fig. 6(a) is rough due to the presence of EG [29]. This result is confirmed by the presence of striations due to the fluidic nature of TiO_2 suspension and the effect of unfavorable capillary and viscous forces related to the physical processes of spin-coating [28, 35]. Several fascinating effects can be observed when TiO_2 NPs sinter

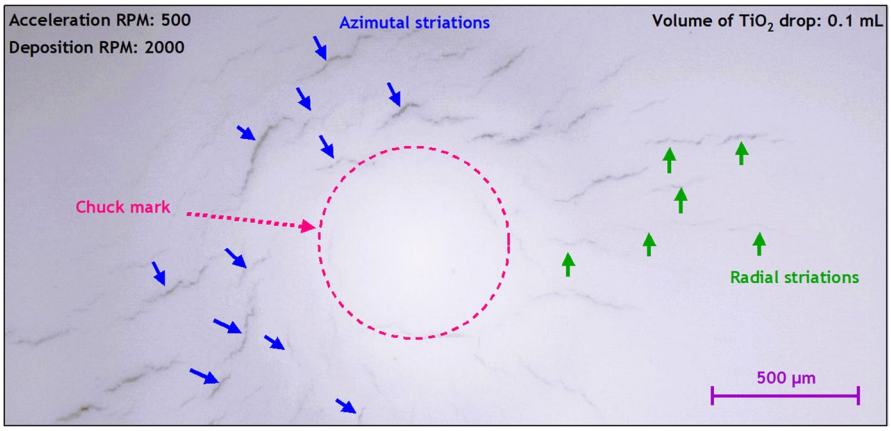

Fig. 5 Effect of acceleration RPM on the striations orientation in the wet TiO_2 film; *i.e.,* azimuthal (blue) and radial (green) striations. The deposition process parameters are shown in the inset

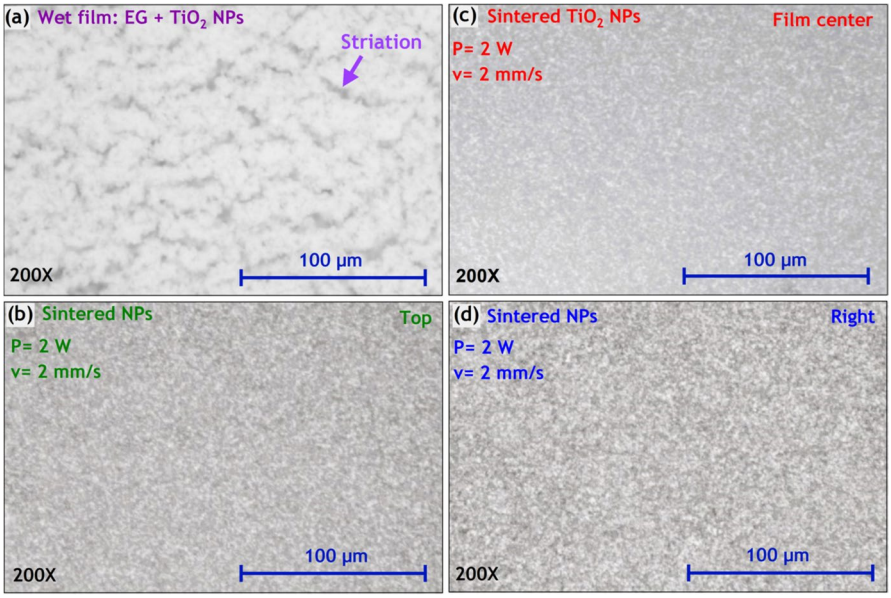

Fig. 6 Optical micrographs of TiO_2 film at various locations. **(a)** As-deposited film (2 *mm* from the film center). **(b)** Top portion. **(c)** Center portion. **(d)** Right portion of the sintered film. An acceleration RPM of 500, and a deposition RPM of 2000 were used

at the laser power 2 *W* and 2 *mm/s* substrate speed [3, 8, 21]. Figure 6(b-d) present the difference in the morphological property of the three sintered portions of the TiO_2 film, *i.e.,* T, C (chuck mark) and R portions. For all portions (T, C and R), the morphology changes from the milky clusters (wet film in Fig. 6(a)) to a compact and solid layer containing sintered nanoparticles (sintered films in Fig. 6(b-d)). The

sintering process also shifts the apparent color compared to that of the wet film, due to the interaction of the film with light of the optical microscope utilized for morphological characterizations [21, 29].

It can be noticed in Fig. 6 that the density of microstructure differs from one sintered portion to another, *e.g.,* $D_{mC} > D_{mT} > D_{mR}$, where D_{mC}, D_{mT} and D_{mR} are the microstructural densities at C (Fig. 6(c)), T (Fig. 6(b)) and R (Fig. 6(d)) respectively. This trend in the microstructural density may be ascribed to the variation of the TiO_2 NPs distribution in the wet film of milky cluster morphology (Fig. 6(a)) formed during the spin coating process. Although the angular speed is the same at any point on the substrate surface, the mass flux of nanoparticles is expected to vary as the radial distance from the center of the film increases and this effect can cause a variation in the distribution of TiO_2 nanoparticles. The distances of portions C, T and R from the film center are $0, 3$ *mm* and 5 *mm*, respectively, which correlates well with the observed variation in the microstructural density, *i.e.,* $D_{mC} > D_{mT} > D_{mR}$.

The variation of density in different portions of the sintered film is examined by measuring the optical transmittance of each portion (R, T and C), asshown in Fig. 7. The portion C shows less transparency (red line) compared to the portions T (green line) and R (blue line). Thistrend in the transmittance can also be ascribed to the variation of the microstructural density. Higher microstructural density at C can correspond to higher opticaldensity, resulting in lower transparency at C as seen in Fig. 7. It is important to note that the variation of the transmittance mayalso be due to the difference in porosity ($Porosity = [1 - Density]\times 100$ [23]) in the five regions. The wet film has lower transmittance because it isthicker than the sintered film. The microstructure density refers to the density of TiO_2 material in the film. The fluidic

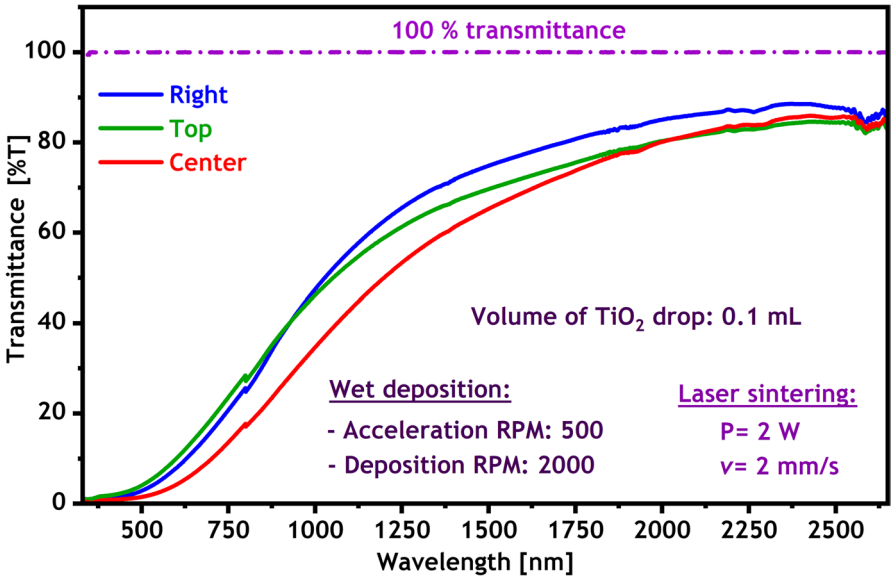

Fig. 7 Measured transmittance from different portions (right, center, and top) of the sintered TiO_2 film. Inset: the processing parameters used for preparing this film

nature of the wet film isconsidered to have insignificant porosity due to the presence of EG and loosely bound NPs. Conversely, the sintered film is considered to have tightly bound NPs andporosity left behind by the evaporated EG. Also the porosity may be caused by the shrinkage of the particles during the sintering process. Higher density of microstructuresimplies more material per unit volume, interacting with the light leading to losses due to scattering and absorption mechanisms [36]. Therefore, the scattering and absorption of incident radiation affect the transmission of light through the film. The microstructural density wasqualitatively examined by measuring the transmittance at various regions of the optical micrographs in Fig. 6. The microstructuraldensity has a significant effect on transmittance, especially in the context of optical and electromagnetic wave propagation through the films [14].

Effect of Laser Sintering on the Microstructures of Films and Transmittance

Laser sintering of TiO_2 nanoparticles is a key step in additive manufacturing technology, and it refers to bonding nanoparticles together to form transparent TiO_2 films with compact morphologies and exceptional optical properties [8, 21]. Laser sintering may also cause fusion of TiO_2 nanoparticles, resulting in both bonding and melting to form compact films [3, 5]. The effect of laser-assisted evaporation and sintering on the microstructures and transmittance of TiO_2 films was also studied. Figure 8(a-c) show the optical micrographs of three (wet, post-evaporated and

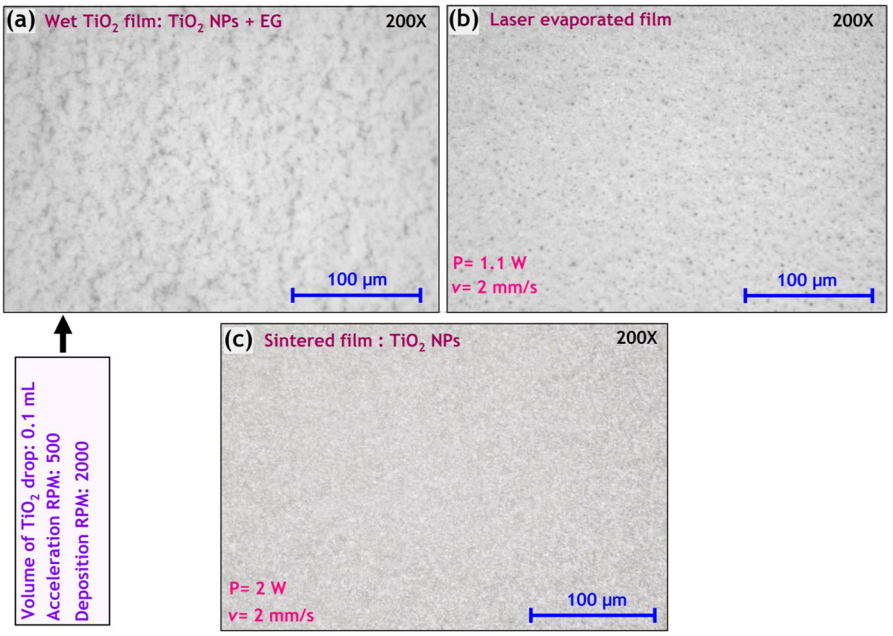

Fig. 8 Optical micrographs of: **(a)** Wet TiO_2 film. **(b)** Film post-evaporation of EG. **(c)** Sintered TiO_2 film. This film was prepared using a deposition RPM of 2000 and an acceleration of 500 RPM

sintered) phases of TiO_2 films. The wet film surface in Fig. 8(a) is rough with milky clusters due to the presence of EG, and this film displays no bonding between nanoparticles [29]. This microstructural feature is confirmed with the SEM micrograph in Fig. 9(a).

As shown in Figs. 8(a) and 9(a), the orientation of the gaps between the clusters, *i.e.,* the striations, corresponds to the direction of the major flow of TiO_2 suspension during the spin-coating deposition of wet films [35]. There is no coalescence and bonding between nanoparticles in the wet film, and the film can be easily removed from the substrate by scratching [29]. Figures 8(b) and 9(b) show the optical and SEM micrographs of the post-evaporation TiO_2 film, respectively. EG is evaporated at $1.1W$ power, resulting in a dry TiO_2 film with roughness less than the original wet film and with the appearance of micropores that may have been produced by the EG vapors escaping from the interior of the wet film [21]. Yang et al. [3] reported that when the size of TiO_2 NPs is much smaller than the laser wavelength, only a fraction of the laser energy can be absorbed by the top layer of the nonsintered TiO_2 film and, therefore, most of the energy can be scattered into the film. They also reported that the interspaces between the nonsintered TiO_2 NPs provide a channel for the propagation of scattered IR light, so the incident laser can penetrate into the film to cause sintering over a deeper region. The densification of the film during laser sintering increases the bonding and coalescence between the TiO_2 nanoparticles in the sintered film, as demonstrated in Fig. 9(c) [3, 21, 27].

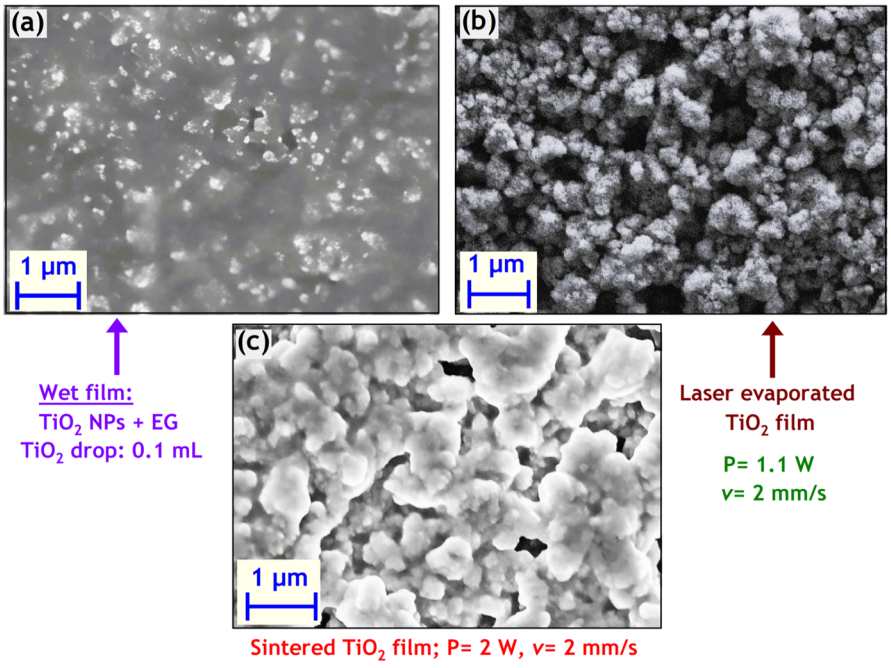

Fig. 9 SEM micrographs of TiO_2 films. **(a)** Wet film. **(b)** Post-evaporated film. **(c)** Sintered film. All images were taken at 2 *mm* from the film center. A deposition RPM of 2000, and an acceleration of 500 RPM were used for spin-coated film shown in (**a**)

The effect of the deposition RPM on the quality of the wet TiO_2 film and striation size is shown in Fig. 10(a). Striation defects are formed due to unfavorable capillary and viscous forces on the NPs suspension during the spreading of the suspension in the spin coating process. The orientation of the striations is related to the direction of the major flow of the suspension [28, 35], and depends on the acceleration, as mentioned earlier in Sect. 4.1. The size of striations increases when the deposition RPM increases (Fig. 10(a)), and consequently, the roughness of the film also increases. This trend may be due to the evaporation-driven surface tension, the variation of the morphology in the wet film when angular speed changes, and the viscosity of the TiO_2 suspension. After sintering, however, the striations disappear, and the film becomes smoother for lower deposition RPM as shown in Fig. 8(c). This result shows the effectiveness of the spin coating deposition followed by laser sintering technique used in this study to deposit transparent films. NELD is suitable for line-by-line deposition of thin films to cover the entire substrate with consecutive lines overlapping on each other, and as a result, the films will not be uniform. Also, NELD can be applied for depositing an array of small dots on different substrates [2, 21].

Shown in Fig. 10(b) is the transmittance of the wet, evaporated, and sintered TiO_2 films. In the UV–Vis spectral range, the transmittance is low for the wet film ($\sim$ 18% maximum) and evaporated film ($\sim$ 40% maximum), which may be due to the absorption of UV–Vis light by the photoexcitation of electrons from the valence band to the conduction band of TiO_2 and may also be due to the effect of the roughness and thickness of the wet film (TiO_2 NPs + EG). The dried TiO_2 film is thicker with rougher surface than that of the sintered film. The rougher surface causes scattering, resulting in less transmission of light into the film. The laser sintering creates smoother surface, resulting in less scattering loss, and higher transmission of light into the film. The transmittance of the sintered film increased from 40% to 62% (at 750 *nm*) in the UV–Vis range and reached a maximum of $\sim$ 95% in the IR region ($\sim$ 2500 *nm*). The transmittance of the wet film reaches a maximum of $\sim$ 78% at 2500 *nm*. This improvement in the transmittance of TiO_2 films (from 78% to 95% in

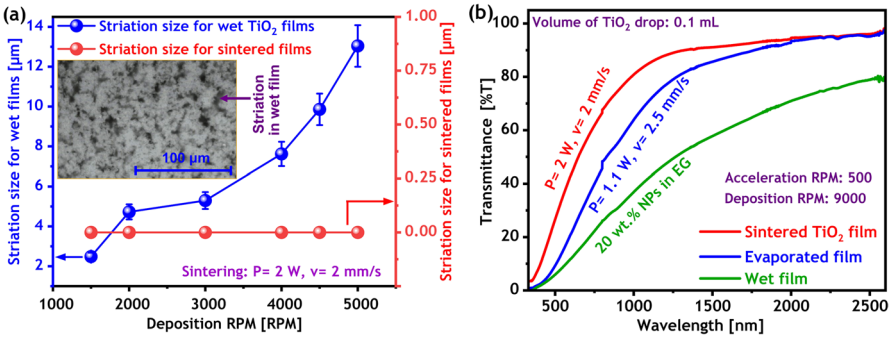

Fig. 10 **(a)** The striation size of the wet TiO_2 film (blue scatters) and of the sintered film (red scatters) as a function of deposition RPM. The micrograph in the inset shows the striations in the wet film. **(b)** Transmittance of wet (green), post-evaporation (blue), and sintered (red) TiO_2 thin films

the IR region) is attributed to the sintering of the nanoparticles, resulting in a thinner dense ceramic layer with a decrease in the thickness of the original layer [3, 8, 21]. The decrement of thickness due the effect of the CO_2 laser processing.

Effect of Spin Coating Speed on the Film Quality and Transmittance

The effect of deposition RPM, or thickness, on the optical morphology and transmittance of the TiO_2 films were studied. The optical micrographs of two films deposited at 2000 RPM and 11000 RPM before sintering are shown in Fig. 11(a) and (c), respectively. The wet film deposited at 2000 RPM shows striations of average width $\sim 2.45\ \mu m$ (Fig. 11(a)), and the wet film deposited at 11000 RPM shows more and larger striations of average width $\sim 16\ \mu m$ (Fig. 11(c)).

The formation of larger striations for the film deposited at 11,000 RPM may be due to the high rate of evaporation of EG at high RPMs and the subsequent changes in the surface tension of the suspension during the spin-coating process. The sintered thick ($h_{SI} = 2.76\ \mu m$) film and thin ($h_{SI} = 0.27\ \mu m$) film show almost no striations due to improved physical coalescence and densification of the nanoparticles during laser sintering [21, 29]. The surfaces of both sintered TiO_2 films (Fig. 11 (b) and (d)) appear to be smoother than the corresponding wet films prepared at two different RPMs. The number and sizes of striations influence the roughness and topography of the sintered films. Sta et al. [23] reported that the roughness of TiO_2 film depends on the film thickness. The effect of the thickness on the transmittance of the sintered TiO_2 films was examined in the range of 330 – 2650 *nm* , as shown in

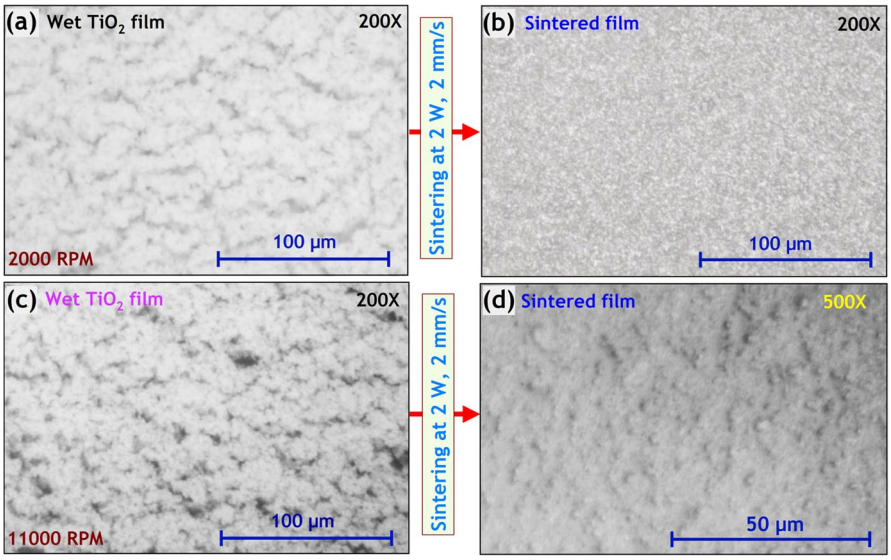

Fig. 11 **(a)** Optical micrograph of wet TiO_2 film deposited at 2000 RPM. **(b)** Film shown in (**a**) after sintering ($h_{SI} = 2.76\ \mu m$). **(c)** Optical micrograph of wet film deposited at 11000 RPM. **(d)** Film shown in (**c**) after sintering ($h_{SI} = 0.27\ \mu m$). An acceleration of 500 RPM was used for depositing both films

Fig. 12. The thick 2.76 μ*m* film exhibits low transmittance (*e.g.,* 4.63 % at 632 *nm*) in the visible spectral range and shows relatively high transmittance (78 % and 2500 *nm*) in the IR region. Conversely, the thin 0.27 μ*m* film shows an enhancement in the transmittance, *i.e.,* from 4.63 % to 45 % at 632 *nm*, and from 78 % to 97 % at 2500 *nm* in the IR region. It is clear that the lower thickness causes this enhancement in the transmittance and, therefore, lower absorptance [37].

Effect of Deposition RPM on Thickness and Transmittance at Various Wavelength Ranges

In this study, transparent anatase TiO_2 films were prepared in the thickness range of $h_{SI} = 0.27\ \mu m$ to $2.76\ \mu m$. The thickness of the spin-coated wet TiO_2 films (h_{SC}) depends on several processing parameters as detailed in Sect. 3.2 [28, 34]. Therefore, the thickness of the sintered TiO_2 film (h_{SI}) depends on h_{SC}. By optimizing acceleration and deposition RPMs, the h_{SI} can be controlled. Figure 13(a) shows the dependency of h_{SI} on the deposition RPM. As the RPM increases from 2000 to 11,000, h_{SI} decreases from 2.76 μ*m* to 0.27 μ*m*, while the transparency of the films increases (Fig. 13(b)). The deposition RPM affects the viscous and centripetal forces during the spin coating process, and thus, affect the thickness, transmittance, and absorptance of TiO_2 films as reported in [35, 37].

As shown in Fig. 13(b), transmittances of 97 %, 96 %, 89 %, 81 % were achieved at 2500 *nm* for sintered TiO_2 films of $h_{SI} = 0.27, 0.55, 1.08$, and $2.14\ \mu m$ thickness, respectively. The transmittance in the visible range increases rapidly as the thickness

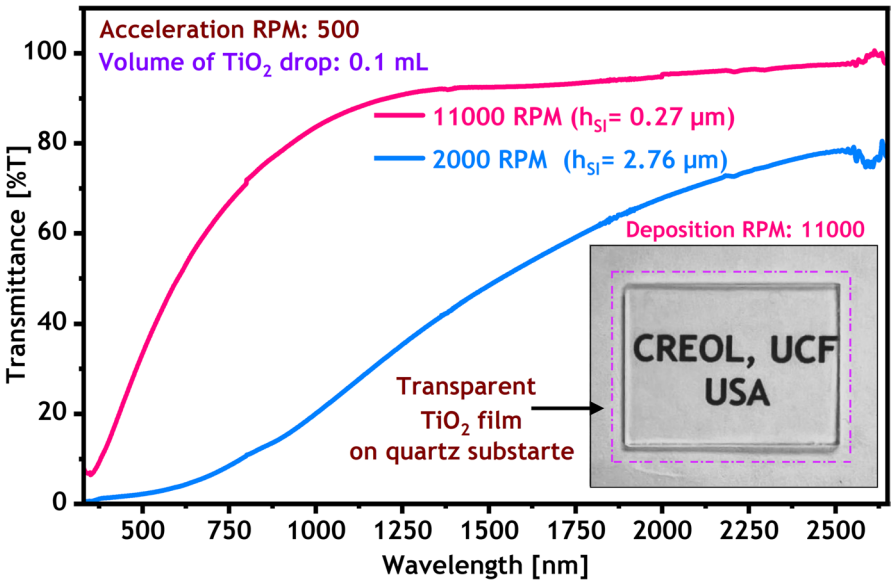

Fig. 12 Comparison in transmittance for thick film (2000 *RPM*, $h_{SI} = 2.76\ \mu m$) and thin TiO_2 film (11000 *RPM*, $h_{SI} = 0.27\ \mu m$). The highly transparent TiO_2 film of 0.27 μm thickness is shown as an inset

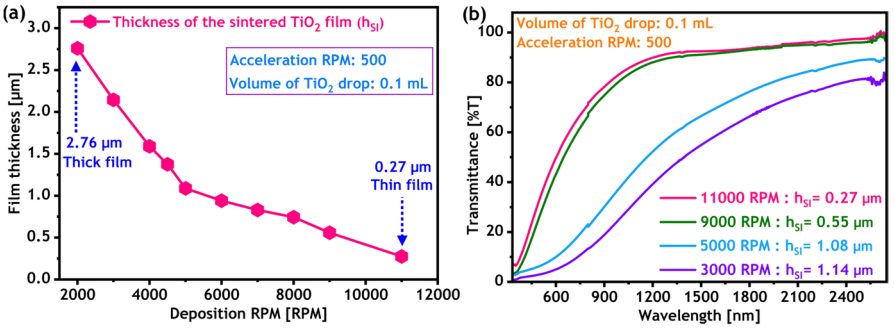

Fig. 13 **(a)** Measured thickness versus deposition RPM. **(b)** Transmittance of the sintered TiO_2 films for different thickness. All TiO_2 films were sintered using 2 W power and 2 mm/s substarte speed

decreases, *e.g.,* from 10.8% for 2.14 μm to 67% for 0.27 μm thickness at 750 nm wavelength, compared to relatively low increment in the infrared region, *e.g.,* from 81 % for 2.14 μm to 97 % for 0.27 μm thickness at 2500 nm wavelength (Fig. 13(b)). This is explained by the fact that the photons of IR light have insufficient energy to interact with the TiO_2 layer compared to the photons of the visible spectrum and, therefore, the infrared photons (*e.g.,* at 2500 nm) can easily transmit through the sintered TiO_2 films [21, 23, 37]. We prepared transparent films starting with milky wet films and sintering TiO_2 NPs, resulting in 92% transmittance (0.55 μm thickness) (Fig. 13). Other studies [8, 38] started with transparent TiO_2 films and thermally sintered to obtain the final films. Mauchauff et al. [38] deposited transparent TiO_2 film of 75 % transmittance (thickness: 0.13 μm) using an open-air hybrid CVD/plasma method. Schade et al. [8] used a UV laser to prepare transparent TiO_2 films of 85 % transmittance (thickness: 0.5 μm). Doubi et al. [39] prepared transparent TiO_2 films of 70 % transmittance (thickness not reported) by chemical spray pyrolysis method.

Using Fourier-transform infrared (FTIR) spectroscopy, we measured the transmittance of a blank fused quartz substrate, and sintered TiO_2 films after depositing the wet films on this substrate at 7000 RPM and 11000 RPM, as shown in Fig. 14(a) in the wavelength range of 2 to 4 μm. In the IR region, both TiO_2 samples have fairly high average transmittance with the highest transmittance occurring in the wavelength range of $2 - 2.5$ μm. Contrary to the UV–Vis-NIR spectrophotometry data described in the previous sections, the FTIR data in Fig. 14 (a) show the measured transmittance for both the quartz substrate and the sintered TiO_2 thin films. Since the performance of the film in practice will involve transmittance, our data are presented as a function of film thickness for general understanding of the effect of thickness.

The FTIR results reveal that the thickness (or deposition RPM) affects the transmittance in the mid-infrared region as well, showing lower transmittance for the lower RPM sample, and this dependency can be explained by the variation of the film thickness. Figure 14(b) shows the transmittance of the sintered TiO_2 films as a function of thickness for different wavelengths. The general trend is that the transmittance increases as the thickness decreases; resulting in less absorbed light because the thinner film does not provide many opportunities for infrared light to

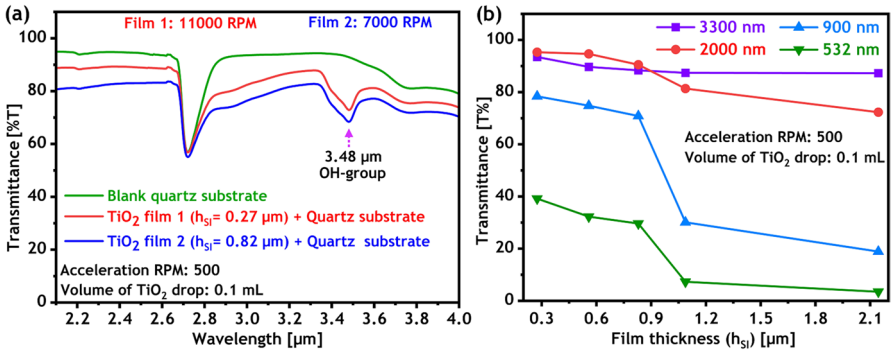

Fig. 14 **(a)** Transmittance from 2 μm to 4 μm using FTIR spectroscopy. **(b)** Transmittance of sintered TiO_2 films as a function of thickness at different wavelength ranges. All TiO_2 films were sintered using 2 W power at 2 mm/s scanning speed

interact with the material, and most of the incident light passes through the film [35, 37]. Conversely, absorptance generally decreases with increasing film thickness, as reported by Domtau et al. [37]. The dip in the absorption peak of the IR spectrum at the 3.4 – 3.5 μm range in Fig. 14(a) is attributed to the presence of hydroxyl (OH) group with strong vibrational modes [40].

Analysis of Structural Properties of TiO_2 Films using XRD Technique

X-ray diffraction (XRD) analysis was carried out to investigate the crystalline structure of TiO_2 films before (wet film) and after laser sintering (Fig. 15(a)). For both the wet and sintered films, the XRD crystalline planes (101), (112), (200), (105), (211), (213), (220) and (215), which are localized at $2\theta = 25°, 37°, 48°, 53°, 55°, 62°, 70°$ and 75° respectively, are found to correlate well to the anatase crystalline phase of

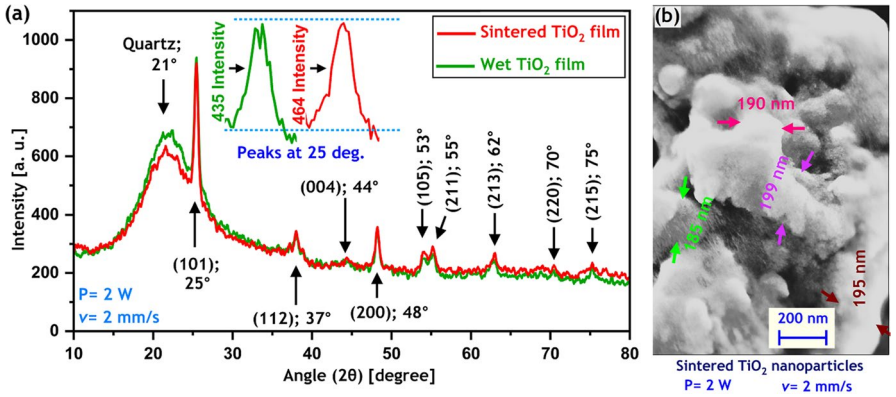

Fig. 15 **(a)** XRD patterns of: (green) wet TiO_2 film, and (red) sintered TiO_2 film deposited on quartz substrate. **(b)** SEM micrograph of the sintered film showing the coalescence and bonding of TiO_2 nanoparticles and the size of sintered crystallites (TiO_2 grains)

TiO_2, as reported previously [21, 23, 41]. These results confirm that both types of films consist of the anatase crystalline phase of TiO_2. The intensity peak around $2\theta = 21°$ [42] corresponds to the peak of the quartz substrate with the wet film and with the sintered TiO_2 film represented by the green and red patterns respectively. It can be seen that the intensity of the sintered sample decreases at $2\theta = 21°$. This trend can be explained by the fact that the sintered film becomes compact causing less penetration of the X-ray radiation through the sintered film to reach the quartz substrate surface than in the case of the wet film that contains striations and pores.

The wet film, thus, allows more penetration of the X-ray radiation thought the wet film to reach the quartz surface. The intensity of the peaks of sintered films at other angles, however, is higher than in the case of wet films because of the bonding of NPs resulting in larger particle sizes with various crystalline orientations. The inset at $2\theta = 25°$ illustrates as an example that the peak intensity of the sintered film is 464 *a.u.* which is higher than the peak intensity (435 *a.u.*) of the wet film. All the XRD peaks of the sintered TiO_2 film ($h_{SI} = 2.76\ \mu m$) correspond to the tetragonal anatase phase of TiO_2 with a space group $I4_1/amd$ (JCPDS78-2486) [23, 41], and the preferred grain orientation corresponds to the dominant (101) plan localized at $2\theta = 25.45°$.

Using the XRD data from Fig. 15(a), the average crystallite size in the sintered TiO_2 film (Fig. 15(b)) is estimated by applying Debye Scherer's equation [23, 26], Eq. (3), to the major peaks of the diffraction patterns, *i.e.,* the peaks located at $2\theta = 25°$, 37°, and 48°, and taking an average of the crystallite sizes $\langle D \rangle$.

$$\langle D \rangle = \frac{K\lambda}{\beta \cos(\theta)} \tag{3}$$

where $\langle D \rangle$ is the average size of TiO_2 crystallites, K is a shape factor taken as 0.94, λ is the wavelength of the X-ray radiation ($CuK\alpha = 1.5406\text{Å}$) used for XRD measurement, β is the FWHM (full width at half maximum) intensity of the peak (in Radian), and θ is the diffraction angle at the position of the peak maximum [23]. The average size of TiO_2 crystallites in the sintered film is found to be $\langle D \rangle \approx 192.25\ nm$. Sintering at high laser power, *e.g.*, 2 *W*, raises the surface temperature of TiO_2 films and, therefore, enhances the interfacial fusion of TiO_2 nanoparticles, resulting in crystallites of larger size as indicated in the SEM micrograph (Fig. 15(b)). This observation agrees with the results obtained by XRD in Fig. 15(a).

Conclusion

Anatase TiO_2 nanoparticle suspension is used to prepare transparent films by a spin-coating technique to create a wet film which is subsequently sintered with a CO_2 laser. The effect of deposition process parameters on the microstructures, transparency and crystalline quality of wet and sintered films is examined. The wet film exhibits milky clusters of nanoparticles with numerous striations representing gaps between the clusters. Laser sintering, however, improves the microstructures of the films by forming a dense layer with enhanced interconnectivity and possibly

localized fusion of the TiO_2 nanoparticles. The wet film can be described as having a rough surface due to the striation defects, whereas the sintered film becomes relatively smoother due to the rearrangements of the atoms and clusters of the nanoparticles. Spectroscopic measurements of transmittance demonstrate that it is possible to prepare transparent anatase TiO_2 thin films with an average transmittance above 92 % in the IR spectral region. XRD data reveal that the crystalline anatase phase of the initial TiO_2 nanoparticle suspension is preserved in the sintered film without any transformation of the anatase phase to the rutile crystalline structure of TiO_2. With the selection of proper laser processing parameters using a simple laser heating model, this study demonstrates an effective laser sintering process for depositing TiO_2 thin films on fused quartz substrates without cracking the substrate and without modifying the crystalline phase of the original nanoparticles. A theoretical model is also presented for relating the deposition RPM used for preparing the wet film to the thickness of sintered films. Experimental data on the sintered film thickness corroborate the theoretical model.

Acknowledgements The authors appreciate the service provided by the Materials Characterization Facility (MCF) for the XRD characterization and SEM imaging, and the CREOL cleanroom for profilometer measurements at UCF. The authors also thank Gunjan Kulkarni for his assistance in experiments and FTIR measurements.

Author Contributions Y. B., A. K., R. K., F. C., and C. J. S. designed and planned the experiments. A. K., R. K., F. C., and C. J. S. were responsible for project planning. Y. B. carried out the experiments, collected the data, and processed the images. Y. B., A. K., and R. K. analyzed the results, co-wrote, and reviewed the manuscript. All authors read and approved the final manuscript.

Funding This work was supported by Naval Air Warfare Center Aircraft Division, IRflex Corporation under Contract No. N6893621C0039 and the Postdoctoral Scholar Program of UCF (P3 Program) under Contract No. 65019B31.

Data Availability All data generated or analyzed during the preparation of this work are included in this article.

Declarations

Competing Interests The authors declare no competing interests.

References

1. Yan, Y., Warren, S.C., Fuller, P., Grzybowski, B.A.: Chemoelectronic circuits based on metal nanoparticles. Nat. Nanotechnol. **11**, 603–608 (2016). https://doi.org/10.1038/nnano.2016.39
2. Castillo, O.E., Kumar, R., Kar, A.: Laser electrospray printing of nanoparticles on flexible and rigid substrates. J. Laser Appl. **31**, 1–6 (2019). https://doi.org/10.2351/1.5079733
3. Yang, H., Liu, W., Xu, C., Fan, D., Cao, Y., Xue, W.: Laser sintering of TiO_2 films for flexible dye-sensitized solar cells. Appl. Sci. **9**, 1–11 (2019). https://doi.org/10.3390/app9050823
4. Fathi, H.P., Johnson, H., Ahmadi, Z., Roach, M., Shamsaei, N., Mahjouri, S.M.: Laser-assisted selective and localized surface transformation of titanium to anatase, rutile, and mixed phase nanostructures. J. Laser Appl. **33**, 1–6 (2021). https://doi.org/10.2351/7.0000316
5. Ming, L., Yang, H., Zhang, W., Zeng, X., Xiong, D., Xu, Z., Wang, H., Chen, W., Xu, X., Wang, M., Duan, J., Cheng, Y.-B., Zhang, J., Bao, Q., Wei, Z., Yang, S.: Selective laser sintering of TiO_2

nanoparticle film on plastic conductive substrate for highly efficient flexible dye-sensitized solar cell application. J. Mater. Chem. A **2**, 4566–4573 (2014). https://doi.org/10.1039/C3TA14210H
6. Takikawa, H., Matsui, T., Sakakibara, T., Bendavid, A., Martin, P.J.: Properties of titanium oxide film prepared by reactive cathodic vacuum arc deposition. Thin Solid Films **348**, 145–151 (1999). https://doi.org/10.1016/S0040-6090(99)00054-1
7. Hanaor, D.A.H., Sorrell, C.C.: Review of the anatase to rutile phase transformation. J. Mater. Sci. **46**, 855–874 (2011). https://doi.org/10.1007/s10853-010-5113-0
8. Schade, L., Franzka, S., Hardt, S., Wiggers, H., Hartmann, N.: Sintering of thin titanium dioxide nanoparticle films via photothermal processing with ultraviolet continuous-wave lasers. Appl. Surf. Sci. **278**, 336–340 (2013). https://doi.org/10.1016/j.apsusc.2012.11.077
9. Li, T., Li, L., Wu. M.: Fabrication and characterization of TiO_2 anti-reflection coatings with gradient index. Micro & Nano Lett. **12**, 849–853 (2017). https://doi.org/10.1049/mnl.2017.0408
10. MirKazem, O., Malekmohammad, M., Zabolian, H.: Wide-angle broadband antireflection coatings based on boomerang-like alumina nanostructures in visible region. Sci. Rep. **12**, 904 (2022). https://doi.org/10.1038/s41598-022-04928-2
11. Euvananont, C., Junin, C., Inpor, K., Limthongkul, P., Thanachayanont, C.: TiO_2 optical coating layers for self-cleaning applications. Ceram. Int. **34**, 1067–1071 (2008). https://doi.org/10.1016/j.ceramint.2007.09.043
12. Sarkın, A.S., Ekren, N., Saglam, S.: A review of anti-reflection and self-cleaning coatings on photovoltaic panels. Sol. Energy **199**, 63–73 (2020). https://doi.org/10.1016/j.solener.2020.01.084
13. Thongsuwan, W., Sroila, W., Kumpika, T., Kantarak, E., Singjai, P.: Antireflective, photocatalytic, and superhydrophilic coating prepared by facile sparking process for photovoltaic panels. Sci. Rep. **12**, 1675 (2022). https://doi.org/10.1038/s41598-022-05733-7
14. Syed, W.A., Rafiq, N., Ali, A., Din, R.U., Shah, W.H.: Multilayer AR coatings of TiO_2/MgF_2 for application in optoelectronic devices. Optik **136**, 564–572 (2017). https://doi.org/10.1016/j.ijleo.2017.02.085
15. Pratima, B.M., Subrahmanyam, A.: Protective coatings on copper using as-deposited sol-gel TiO_2-SiO_2 films. Materials Today: Proceedings **80**, 1061–1065 (2023). https://doi.org/10.1016/j.matpr.2022.11.463
16. Bougdid, Y., Maouli, I., Rahmouni, A., Mochizuki, K., Bennani, I., Halim, M., Sekkat, Z.: Systematic λ21 resolution achieved in nanofabrication by two photon-absorption induced polymerization. J. Micromech. Microeng. **29**, 1–7 (2019). https://doi.org/10.1088/1361-6439/aafda0
17. Bougdid, Y., Sekkat, Z.: Voxels optimization in 3D laser nanoprinting. Sci. Rep. **10**, 1–8 (2020). https://doi.org/10.1038/s41598-020-67184-2
18. Bougdid, Y., E.l., Idrissi, Y., Maouli, I., Sekkat Z.: Direct laser writing of submicrometric voxels in two-photon photopolymerization. Proc. of SPIE 11098, Molecular and Nano Machines II, 110980 (2019). https://doi.org/10.1117/12.2528439
19. Moujdi, S., Bougdid, Y., Rahmouni, A., Mahfoud, T., Nesterenko, D., Halim, M., Sekkat, Z.: Azopolymers for holographic recording: Photo-assisted holography and surface relief gratings. Proc. of SPIE 10944, Practical Holography XXXIII: Displays, Materials, and Applications, 1094403 (2019). https://doi.org/10.1117/12.2513416
20. Castillo, O.E., Kumar, R., Kar, A.: Laser-induced subwavelength structures by microdroplet superlens. Opt. Express **27**, 8130–8142 (2019). https://doi.org/10.1364/OE.27.008130
21. Bougdid, Y., Chenard, F., Sugrim, J., Kumar, R., Kar, A.: CO_2 laser-assisted sintering of TiO_2 nanoparticles for transparent films. J. Laser App. **35**, 1–11 (2022). https://doi.org/10.2351/7.0000821
22. Chenard, F., Alvarez, O., Buff, A. K., Regmi, A. R., Bougdid, Y., Kar, A. Kumar, R.: 3D laser deposition of inorganic transparent materials for advanced optics. IEEE Re. Appl. Photon. Defense Conf. (RAPID), 1–2 (2022). https://doi.org/10.1109/RAPID54472.2022.9911264
23. Sta, I., Jlassi, M., Hajji, M., Boujmil, M.F., Jerbi, R., Kandyla, M., Kompitsas, M., Ezzaouia, H.: Structural and optical properties of TiO_2 thin films prepared by spin-coating. J. Sol gel Sci. Technol. **72**, 421–427 (2014). https://doi.org/10.1007/s10971-014-3452-z
24. Schade, L., Franzka, S., Thomas, M., Hagemann, U., Hartmann, N.: Resonant laser processing of nanoparticulate Au/TiO_2 films on glass supports: Photothermal modification of a photocatalytic nanomaterial. Surf. Sci. **650**, 57–63 (2016). https://doi.org/10.1016/j.susc.2016.01.006
25. Radovic, M., Dubourg, G., Kojic, S., Dohcevic, M.Z., Stojadinovic, B., Bokorov, M., Crnojevic, B.V.: Laser sintering of screen-printed TiO_2 nanoparticles for improvement of mechanical and electrical properties. Ceram. Int. **44**, 10975–10983 (2018). https://doi.org/10.1016/j.ceramint.2018.03.181

26. Bakri, A.S., Sahdan, M.Z., Adriyanto, F., Raship, N.A., Said, N.D.M., Abdullah, S.A., Rahim, M.S.: Effect of annealing temperature of titanium dioxide thin films on structural and electrical properties. AIP Conf. Proc. **1788**, 030030 (2017). https://doi.org/10.1063/1.4968283
27. Cheng, J., Kar, A.: Studies for laser densification of ceramic coating. Mater. Manuf. Process. **12**, 487–503 (2007). https://doi.org/10.1080/10426919708935159
28. Tyona, M.D.: A theoretical study on spin coating technique. Adv. Mater. Res. **2**, 195–208 (2013). https://doi.org/10.12989/AMR.2013.2.4.195
29. Bougdid, Y., Chenard, F., Sugrim, J., Kumar, R., Kar, A.: Transmittance of TiO_2 nanoparticle-based films deposited by CO_2 laser heating. Proc. SPIE 12412, Laser 3D Manufact. **X**, 1241209 (2023). https://doi.org/10.1117/12.2647981
30. Sani, E., Dell'Oro, A.: Optical constants of ethylene glycol over an extremely wide spectral range. Opt. Mater. **37**, 36–41 (2014). https://doi.org/10.1016/j.optmat.2014.04.035
31. Incropera, F. P., De-Witt, D. P.: Fundamentals of heat and mass transfer, 2nd edition. United States: John Wiley and Sons Inc.**,** New York, p. 203 (1985). Fundamentals of heat and mass transfer, 2nd edition (Book) | OSTI.GOV
32. Prokhorov, A. M., Konov, V. I., Ursu, I., Mihailescu, I. N.: Laser heating of metals. English Edition, IOP Publishing, New York, p. 43 (1990). https://doi.org/10.1201/9781351073943
33. Mufti, N., Laila, I. K. R., Hartatiek, Fuad, A.: The effect of TiO_2 thin film thickness on self-cleaning glass properties. IOP Conf. Series: J. Phys.: Conf. Series. **853**, 1–7 (2017). https://doi.org/10.1088/1742-6596/853/1/012035
34. Flores, J. D., Eickelmann, S., Riegler. H.: Evaporation behavior of a thinning liquid film in a spin coating setup: Comparison between calculation and experiment. Eng. Rep. **3**, 1–12 (2021). https://doi.org/10.1002/eng2.12390
35. Dunbar, P., Birnie III.: Rational solvent selection strategies to combat striation formation during spin coating of thin films. J. Mater. Res. **16**, 145–1154 (2001). https://doi.org/10.12989/amr.2013.2.4.195
36. Abdellatif, S., Sharifi, P., Kirah, K., Ghannam, R., Khalil, A.S.G., Erni, D., Marlow, F.: Refractive index and scattering of porous TiO_2 films. Microporous Mesoporous Mater. **264**, 84–91 (2018). https://doi.org/10.1016/j.micromeso.2018.01.011
37. Domtau, D. L., Simiyu, J., Ayieta, E. O., Muthoka, B., Mwabora, J. M.: Optical and electrical properties dependence on thickness of screen-printed TiO_2 thin films. J. Mat. Phy. Chem. **4**, 1–3 (2016). https://doi.org/10.12691/jmpc-4-1-1
38. Mauchauffe, R., Kim, J., Kim, D.H., Lee, S., Kwon, M., Moon, S.Y.: UV-Shielding TiO_2 thin film deposition on flexible and heat-labile substrate using an open-air hybrid CVD/Plasma method. Vacuum **192**, 110424 (2021). https://doi.org/10.1016/j.vacuum.2021.110424
39. Doubi, Y., Hartiti, B., Siadat, M., Nkuissi, H.J.T., Labrim, H., Fadili, S., et al.: The effect of experimental process on properties of pure TiO_2 nanostructure for fast NO_2 gas sensor. Appl. Phys. A **128**, 463 (2022). https://doi.org/10.1007/s00339-022-05611-z
40. Enas, M.A., Magdy, A.H.Z., Fatma, S.A., Abd Elhady, S.A., Samah, S.N.: Synthesis and swelling characterization of carboxymethyl cellulose -g- poly(acrylic acid- co –acrylamide) hydrogel and their application in agricultural field. Int. J. ChemTech Res. **9**, 270–281 (2016)
41. Ghadiry, M., Gholami, M., Lai, K., Ahmad, H., Chong, W.Y.: Ultra-sensitive humidity sensor based on optical properties of graphene oxide and nano-anatase TiO_2. PLoS ONE **11**, 1–14 (2016). https://doi.org/10.1371/journal.pone.0153949
42. Sun, J., Xu, Z., Li, W., Shen, X.: Effect of nano-SiO_2 on the early hydration of alite-sulphoaluminate cement. Nanomaterials **7**, 1–15 (2017). https://doi.org/10.3390/nano7050102